Editors' Suggestion

QCD Equation of State of Dense Nuclear Matter from a Bayesian Analysis of Heavy-Ion Collision Data

Manjunath Omana Kuttan,[1,2,3,*] Jan Steinheimer,[1,†] Kai Zhou,[1,‡] and Horst Stoecker[1,2,4,§]
[1]Frankfurt Institute for Advanced Studies, Ruth-Moufang-Strasse 1, D-60438 Frankfurt am Main, Germany
[2]Institut für Theoretische Physik, Goethe Universität Frankfurt, Max-von-Laue-Strasse 1, D-60438 Frankfurt am Main, Germany
[3]Xidian-FIAS International Joint Research Center, Giersch Science Center, D-60438 Frankfurt am Main, Germany
[4]GSI Helmholtzzentrum für Schwerionenforschung GmbH, Planckstrasse 1, D-64291 Darmstadt, Germany

(Received 14 December 2022; revised 24 April 2023; accepted 18 October 2023; published 16 November 2023)

Bayesian methods are used to constrain the density dependence of the QCD equation of state (EOS) for dense nuclear matter using the data of mean transverse kinetic energy and elliptic flow of protons from heavy ion collisions (HICs), in the beam energy range $\sqrt{s_{\mathrm{NN}}} = 2$–$10$ GeV. The analysis yields tight constraints on the density dependent EOS up to 4 times the nuclear saturation density. The extracted EOS yields good agreement with other observables measured in HIC experiments and constraints from astrophysical observations both of which were not used in the inference. The sensitivity of inference to the choice of observables is also discussed.

DOI: 10.1103/PhysRevLett.131.202303

The properties of dense and hot nuclear matter, governed by the strong interaction under quantum chromodynamics (QCD), is an unresolved, widely studied topic in high energy nuclear physics. First principle lattice QCD studies, at vanishing and small baryon chemical potential, predict a smooth crossover transition from a hot gas of hadronic resonances to a chirally restored phase of strongly interacting quarks and gluons [1,2]. However, at high net baryon density, i.e., large chemical potential, direct lattice QCD simulations are at present not available due to the fermionic sign problem [3]. Therefore, QCD motivated effective models as well as direct experimental evidence are employed to search for structures in the QCD phase diagram such as a conjectured first or second order phase transition and a corresponding critical endpoint [4–6]. Diverse signals had been suggested over the last decades [7–11], but a conclusive picture has not emerged yet due to a lack of systematic studies to relate all possible signals to an underlying dynamical description of the system, both consistently and quantitatively.

Recently, both machine learning and Bayesian inference methods have been employed to resolve this lack of unbiased quantitative studies. A Bayesian analysis has shown that the hadronic flow data in ultrarelativistic heavy-ion collisions at the LHC and RHIC favor an EOS similar to that calculated from lattice QCD at vanishing baryon density [12]. In the high density range where lattice QCD calculations are not available, deep learning models are able to distinguish scenarios with and without a phase transition using the final state hadron spectra [13–17].

This Letter presents a Bayesian method to constrain quantitatively the high net baryon density EOS from data of intermediate beam energy heavy-ion collisions. A recent study has attempted such an analysis by a rough, piecewise constant speed of sound parameterization of the high density EOS [18]. In this Letter, a more flexible parameterization of the density dependence of the EOS is used in a model which can incorporate this density dependent EOS in a consistent way and then make direct predictions for different observables.

In this Letter, the dynamic evolution of heavy-ion collisions is entirely described by the microscopic Ultrarelativistic Quantum Molecular Dynamics (UrQMD) model [19,20] which is augmented by a density dependent EOS. This approach describes the whole system evolution consistently within one model. No parameters besides the EOS itself are varied here.

UrQMD is based on the propagation, binary scattering, and decay of hadrons and their resonances. The density dependent EOS used in this model is realized through an effective density dependent potential entering in the nonrelativistic quantum molecular dynamics (QMD) [7,21,22] equations of motions,

$$\dot{\mathbf{r}}_i = \frac{\partial \mathbf{H}}{\partial \mathbf{p}_i}, \qquad \dot{\mathbf{p}}_i = -\frac{\partial \mathbf{H}}{\partial \mathbf{r}_i}. \tag{1}$$

Here $\mathbf{H} = \sum_i H_i$ is the total Hamiltonian of the system including the kinetic energy and the total potential energy

$\mathbf{V} = \sum_i V_i \equiv \sum_i V(n_B(r_i))$. The equations of motion are solved given the potential energy V, which is related to the pressure in a straightforward manner [23]

$$P(n_B) = P_{\mathrm{id}}(n_B) + \int_0^{n_B} n' \frac{\partial U(n')}{\partial n'} dn'. \tag{2}$$

Here, $P_{\mathrm{id}}(n_B)$ is the pressure of an ideal Fermi gas of baryons and $U(n_B) = [\partial(n_B \cdot V(n_B))/\partial n_B]$ is the single particle potential. Evidently, the potential energy is directly related to the EOS and therefore the terms potential energy and EOS are interchangeably used in this Letter.

This model assumes that only baryons are directly affected by the potential interaction [24]. A much more detailed description of the implementation of the density dependent potential can be found in [23,25]. Note that this method does yield for bulk matter properties, strikingly similar results as the relativistic hydrodynamics simulations when the same EOS is used [25].

To constrain the EOS from data, a robust and flexible parameterization for the density dependence of the potential energy that is capable of constructing physical equations of state (EOSs) is necessary. For densities below twice the nuclear saturation density (n_0), the EOS is reasonably constrained by the QCD chiral effective field theory (EFT) calculations [26,27], data on nuclear incompressibility [28], flow measurements at moderate beam energies [7,29–31], and Bayesian analysis of both neutron star observations and low energy heavy-ion collisions [32]. This Letter focuses on the high density EOS, particularly in the range $2n_0$–$6n_0$, which is not well understood yet. Therefore, the potential energy $V(n_B)$ is fixed for densities up to $2n_0$ by using the chiral mean field (CMF) model fit to nuclear matter properties and flow data in the low beam energy region [23]. For densities above $2n_0$, the potential energy per baryon V is parameterized by a seventh degree polynomial:

$$V(n_B) = \sum_{i=1}^{7} \theta_i \left(\frac{n_B}{n_0} - 2\right)^i + h \tag{3}$$

where $h = -22.07$ MeV is set to ensure that the potential energy is a continuous function at $2n_0$.

This Letter constrains the parameters θ_i and thus the EOS, via Bayesian inference, using the elliptic flow v_2 and the mean transverse kinetic energy $\langle m_T \rangle$-m_0 of midrapidity protons in Au-Au collisions at beam energy $\sqrt{s_{\mathrm{NN}}} \approx$ 2–10 GeV. The v_2 data are from midcentral collisions at $\sqrt{s_{\mathrm{NN}}} = 2.24$, 2.32, 2.4, 2.42, 2.51, 3.0, 3.32, 3.84, 4.23, and 4.72 GeV [33–39] and the $\langle m_T \rangle$-m_0 data are from central collisions at $\sqrt{s_{\mathrm{NN}}} = 3.83$, 4.29, 6.27, 7.7, and 8.86 GeV [40–42]. Important, sensitive observables such as the directed flow [9,43] are then used to cross check the so extracted EOS. The choice of proton observables (as proxy to baryons) is due to the fact that interesting features in the EOS at high baryon density and moderate temperatures are dominated by the interactions between baryons and protons form the most abundant hadron species, actually measured in experiments, for beam energies considered in the present work. Further details on the choice of data and calculation of flow observables are given in the Supplemental Material [44], which includes Ref. [45].

The experimental data $\mathbf{D} = \{v_2^{\mathrm{exp}}, \langle m_T \rangle^{\mathrm{exp}}\text{-}m_0\}$ are used to constrain the parameters of the model $\boldsymbol{\theta} = \{\theta_1, \theta_2, \ldots, \theta_7\}$ by using the Bayes theorem, given by

$$P(\boldsymbol{\theta}|\mathbf{D}) \propto P(\mathbf{D}|\boldsymbol{\theta}) P(\boldsymbol{\theta}). \tag{4}$$

Here $P(\boldsymbol{\theta})$ is the prior distribution, encoding our prior knowledge on the parameters while $P(\mathbf{D}|\boldsymbol{\theta})$ is the likelihood for a given set of parameters which dictates how well the parameters describe the observed data. Finally, $P(\boldsymbol{\theta}|\mathbf{D})$ is the desired posterior which codifies the updated knowledge on the parameters $\boldsymbol{\theta}$ after encountering the experimental evidence $\mathbf{D}$.

The objective is to construct the joint posterior distribution for the seven polynomial coefficients ($\boldsymbol{\theta}$) based on experimental observations, for which Markov chain Monte Carlo (MCMC) sampling methods are used. For an arbitrary parameter set, the relative posterior probability up to an unknown normalization factor is simply given by the prior probability as weighted by its likelihood. To evaluate the likelihood for a parameter set, the v_2 and the $\langle m_T \rangle$-m_0 observables need to be calculated by UrQMD. The MCMC method then constructs the posterior distribution by exploring the high-dimensional parameter space based on numerous such likelihood evaluations. This requires numerous computationally intensive UrQMD simulations which would need unfeasible computational resources. Hence, Gaussian process (GP) models are trained as fast surrogate emulators for the UrQMD model, to interpolate simulation results in the parameter space [12,46–48]. Cuts in rapidity and centrality that align with that of the experiments are applied on UrQMD data to create training data for the GP models. The constraints applied to generate the physical EOSs to train the models, the performance of the GP models, and other technical details can be found in the Supplemental Material.

The prior on the parameter sets is chosen as Gaussian distributions with means and variances evaluated under physical constraints. More details on the choice of the priors are given in the Supplemental Material. The log-likelihood is evaluated using uncertainties from both the experiment and from the GP model. The prior, together with the trained GP emulator, experimental observations, and the likelihood function are used for the MCMC sampling by employing the DeMetropolisZ [49,50] algorithm from PyMCv4.0 [51].

Closure tests.—In order to verify the performance of the Bayesian inference method described above, two closure

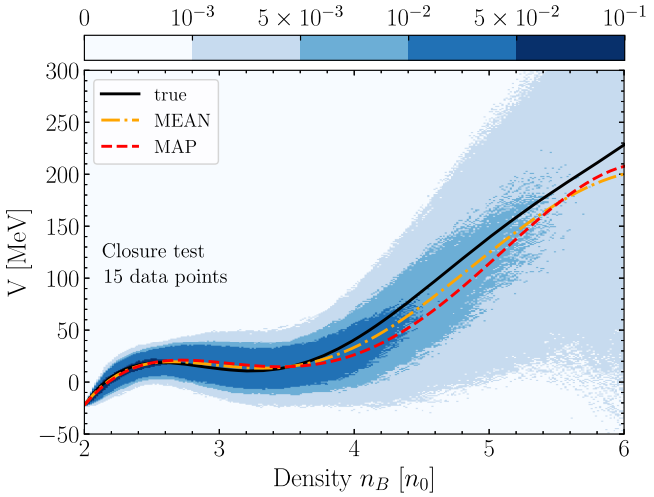

FIG. 1. Visualization of the sampled posterior in the closure test. The color represents the probability for the potential at a given density. The ground-truth EOS used for generating the observations is plotted as a black solid line. The red dashed and orange dot-dashed curves are the MAP and MEAN EOS for the posterior.

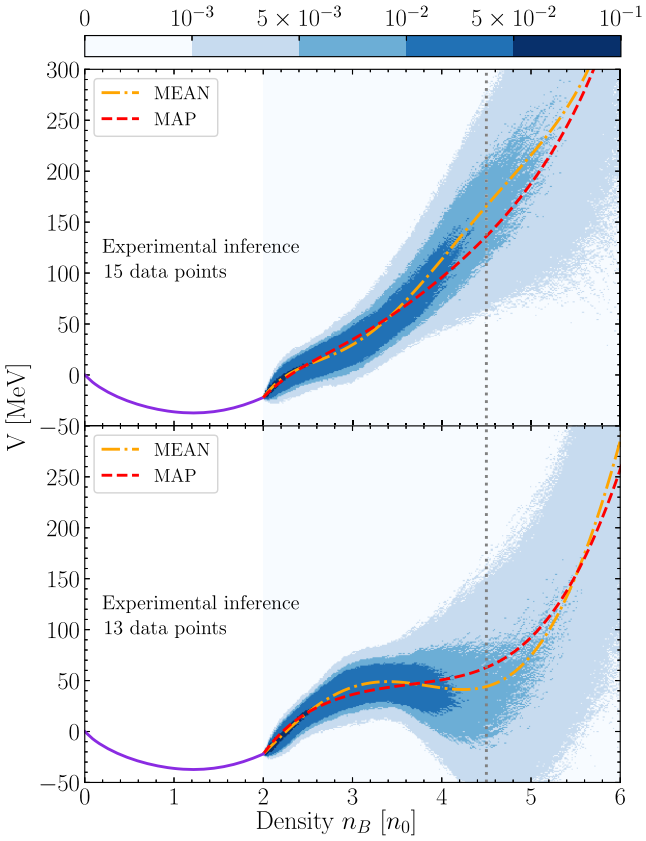

FIG. 2. Posterior distribution for the EOS inferred using experimental observations of v_2 and $\langle m_T \rangle$-m_0. The top figure is the posterior when all 15 data points were used while the bottom figure is obtained without using the $\langle m_T \rangle$-m_0 values for $\sqrt{s_{\mathrm{NN}}} = 3.83$ and 4.29 GeV. The MAP and MEAN EOSs in both cases are plotted in red dashed and orange dot-dashed curves, respectively. The vertical, gray line depicts the highest average central compression reached in collisions at $\sqrt{s_{\mathrm{NN}}} = 9$ GeV. The CMF EOS is plotted in violet for density below $2n_0$.

tests are performed. The first test involves constructing the posterior using v_2 and $\langle m_T \rangle$-m_0, simulated with the experimental uncertainties from UrQMD for a specific but randomly chosen EOS. The inference results are then compared to the known "ground truth." Figure 1 shows the posterior constructed in one such test for a random input potential. The black curve in the plot is the ground-truth input potential while the color contours represent the reconstructed probability density for a given value of the potential $V(n_b)$. Two specific estimates of the ground-truth potential are highlighted in the figure besides the posterior distribution of the potential. These are the maximum *a posteriori* (MAP) estimate, which represents the mode of the posterior distribution as evaluated via MCMC and the "MEAN" estimate as calculated by averaging the values of the sampled potentials at different densities. The comparison of the MAP and the MEAN curves with the ground truth shows that the reconstruction results from the Bayesian inference are centered around the ground-truth EOS and the sampling converges indeed to the true posterior. From the spread of the posterior it can be seen that the EOS in the closure test is well constrained up to densities $4n_0$ for the observables used in the present Letter. For densities from $4n_0$ up to $6n_0$ the generated EOSs have larger uncertainties. However, the mean potentials follow closely the true potential.

The second closure test is done in order to determine the sensitivity of the inference to the choice of the observational data. Hence, the procedure is similar to the previous test, except that the $\langle m_T \rangle$-m_0 values for $\sqrt{s_{\mathrm{NN}}} = 3.83$ and 4.29 GeV are not used in this test to estimate the posterior. When these two data points are excluded, the agreement of the ground-truth EOS with the MAP and MEAN estimates decreases considerably for densities greater than $4n_0$. This indicates that these data points are crucial indeed for constraining the EOS at higher densities. Further details about these closure tests, and the sensitivity on excluding different data points, can be found in the Supplemental Material. There, also a comparison of the prior and posterior probability distributions is shown to highlight the actual information gain obtained through the Bayesian inference.

Results based on experimental data.—The results of sampling the posteriors by using experimental data, for the two cases, with and without the $\langle m_T \rangle$-m_0 values at $\sqrt{s_{\mathrm{NN}}} = 3.83$ and 4.29 GeV, are shown in Fig. 2. The upper panel corresponds to using 15 experimental data points while the lower panel shows the results without the two $\langle m_T \rangle$-m_0 values. The data as used in this Letter do well constrain the EOS, for densities from $2n_0$ to $4n_0$. However, beyond $4n_0$, the sampled potentials have a large uncertainty and the variance is significantly larger for the posterior extracted

from 13 data points. Beyond densities of about $3n_0$, the posterior extracted using 13 data points differs significantly from the posterior extracted using all 15 points. This is quite different from our closure tests, where the extracted MAP and MEAN curves did not depend strongly on the choice of the data points used. This indicates a possible tension within the data in the context of the model used.

To understand this significant deviation which appears when only two data points are removed, the MAP and MEAN EOS resulting from the two scenarios are implemented into the UrQMD model to calculate the v_2 and $\langle m_T \rangle$-m_0 values which are then compared with the experimental data which were used to constrain them. Figure 3 shows the MAP and MEAN curves together with 1-sigma confidence intervals from the posterior. Both results, with different inputs, fit the v_2 data very well except for the small deviation at the high energies. The fit is slightly better when the $\langle m_T \rangle$-m_0 values at the lowest energies are removed. At the same time, using all data point results in larger $\langle m_T \rangle$-m_0 values for both the MAP and MEAN curves. The bands for $\langle m_T \rangle$-m_0 are much broader than the bands for v_2. Yet, the uncertainty bands clearly support the differences in the fit portrayed by the MEAN and MAP curves. The model encounters a tension between the $\langle m_T \rangle$-m_0 and the v_2 data. This tension may either be due to a true tension within the experimental data, or due to a shortcoming of the theoretical model used to simulate both the $\langle m_T \rangle$-m_0 and the v_2 data at high beam energies for a given equation of state. It should also be noted that at higher beam energies the contributions from the mesonic degrees of freedom to the equation of state become more dominant which may make an explicitly temperature dependent equation of state necessary.

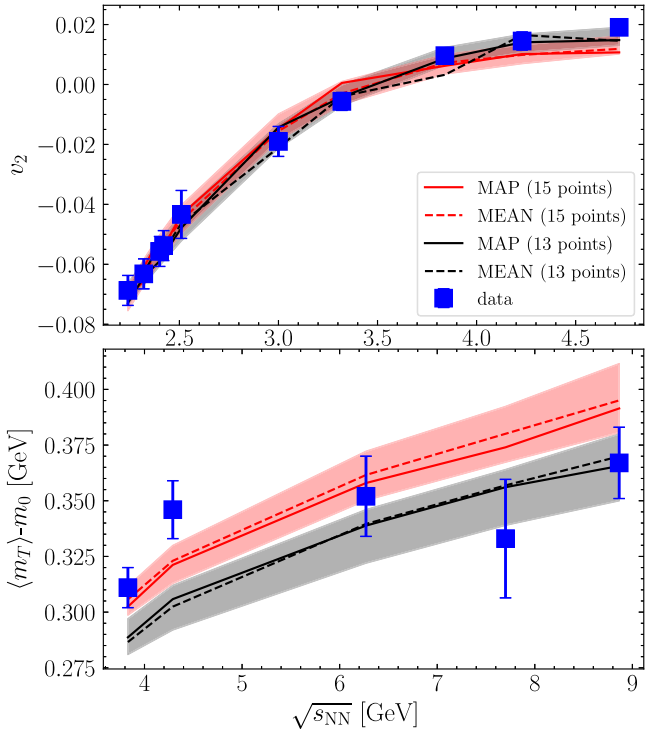

FIG. 3. v_2 and $\langle m_T \rangle$-m_0 values from UrQMD using the MEAN and MAP EOS as extracted from measured data. The observables for both MAP and MEAN EOSs, extracted by using all 15 data points are shown as solid and dashed red lines, respectively, while those generated using only the 13 data points are shown as solid and dashed black lines, respectively. The experimental data are shown as blue squares. The uncertainty bands correspond to a 68% credibility constraint constructed from the posterior samples.

Finally, the extracted EOS can be tested using various observables like differential flow measurements (see Supplemental Material, which include Refs. [52–56]) or different flow coefficients. The slope of the directed flow dv_1/dy at midrapidity are calculated using the reconstructed MEAN and MAP EOSs. The results together with available experimental data are shown in Fig. 4. The dv_1/dy prediction closely matches the experimental data, especially at the higher energies, for the MEAN EOS extracted from all 15 data points. The 1-sigma confidence intervals are indicated as colored bars. It is shown only for one beam energy due to the high computational cost. It can be seen that at high energies, in the 13-point case, the prediction clearly undershoots the data while in the 15-points case, the experimental data lie at the border of the 1-sigma band. The reconstructed EOSs for all other energies are consistent with the dv_1/dy data though it was not used to constrain the EOSs.

To relate the extracted high density EOS to constraints from astrophysical observations, the squared speed of sound (c_s^2) at $T = 0$ is presented for the MEAN EOSs as a function of the energy density in Fig. 5, together with a contour which represents the constraints from recent binary neutron star merger (BNSM) observations [61,62]. The speed of sound, as the derivative of the pressure, is very sensitive to even small variations of the potential energy. The c_s^2 values estimated from all data points show overall

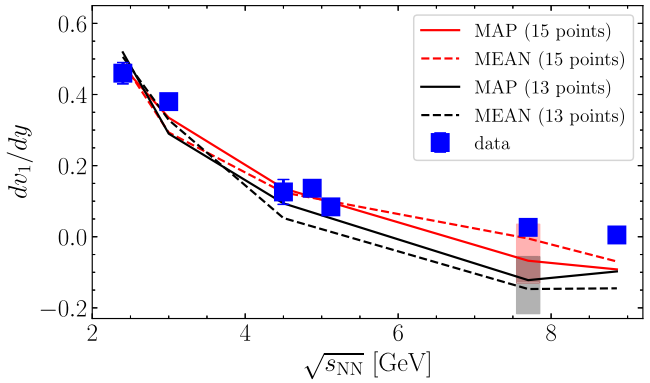

FIG. 4. Slope of the directed flow, dv_1/dy, of protons at midrapidity. The experimental data [37–39,56–60] are shown as blue squares. The colored bars correspond to a 68% credibility constraint constructed from the posterior samples.

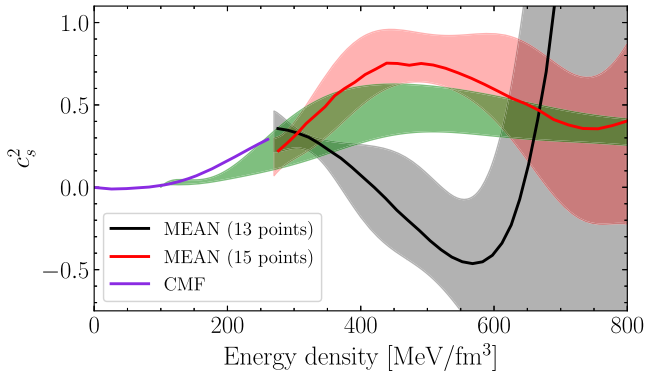

FIG. 5. Speed of sound squared c_s^2, at $T = 0$, as a function of energy density. The c_s^2 for the MEAN EOS extracted from all data points are shown in red and those extracted from only 13 data points are shown in black. The constraints from astrophysical observations are shown as a green band. For energy densities up to 270 MeV/fm^3, the speed of sound from the CMF is plotted as a violet curve. The uncertainty bands correspond to a 68% credibility constraint from the inferred potential curves.

agreement with the c_s^2 constraints from astrophysical observations and predict a rather stiff equation of state at least up to $4n_0$. In particular, both the astrophysical constraints (see also [63]) and the EOS inference in the present work gives a broad peak structure for c_s^2. This is compatible with recent functional renormalization group (FRG) [64] and conformality [65] analyses. However, if only the 13 data points are used, the extracted speed of sound shows a drastic drop, consistent with a strong first order phase transition at high densities [8,9]. This is consistent with the softening phenomenon observed for $\langle m_T \rangle$-m_0 data shown in Fig. 3. In order to give an estimate of the uncertainty on the speed of sound, we have calculated the speed of sound for 100 000 potentials which lie within the 68% credibility interval of the coefficients, however, excluding those which lead to acausal equations of state for densities below 4.5 n0.

Conclusion.—Bayesian inference can constrain the high density QCD EOS using experimental data on v_2 and $\langle m_T \rangle$-m_0 of protons. Such an analysis, based on HIC data, can verify the dense QCD matter properties extracted from neutron star observations and complements astrophysical studies to extract the finite temperature EOS from BNSM merger signals as well as constrain its dependence on the symmetry energy.

A parametrized density dependent potential is introduced in the UrQMD model used to train Gaussian process models as fast emulators to perform the MCMC sampling. In this framework, the input potential can be well reconstructed from experimental HIC observables available already now from experimental measurements. The experimental data constrain the posterior constructed in our method for the EOS, for densities up to $4n_0$. However, beyond $3n_0$, the shape of the posterior depends on the choice of observables used. As a result, the speed of sound extracted for these posteriors exhibit obvious differences. The EOS extracted using all available data points is in good agreement with the constraints from BNSMs with a stiff EOS for densities up to $4n_0$ and without a phase transition. A cross-check is performed with the extracted potentials by calculating the slope of the directed flow. Here, a MEAN potential extracted from all 15 data points gives the best, consistent description of all available data. The inferences encounter a tension in the measurements of $\langle m_T \rangle$-m_0 and v_2 at a collision energy of $\approx$4 GeV. This could indicate large uncertainties in the measurements, or alternatively the inability of the underlying model to describe the observables with a given input EOS. Note, that the data are from different experiments that have been conducted during different time periods. The differences in the acceptances, resolutions, statistics, and even analysis methods of experimental data make it difficult for us to pin down the exact sources of these effects.

Tighter constraints and fully conclusive statements on the EOS beyond density $3n_0$ require accurate, high statistics data in the whole beam energy range of 2–10 GeV which will hopefully be provided by the beam energy scan program of STAR-FXT at RHIC, the upcoming CBM experiment at FAIR, and future experiments at HIAF and NICA. It is noted that, when approaching higher beam energies, which would be important in extending the constraints to higher temperatures and/or densities, the currently used transport model needs to incorporate further finite-temperature and possible partonic matter effects together with relativistic corrections, which we leave for future studies. Further effort should be put into the development and improvement of the theoretical models to consistently incorporate different density dependent EOSs for the study of systematic uncertainties [66]. In the future, the presented method can also be extended to include more parameters of the model as free parameters for the Bayesian inference, which would also require more and precise input data. In addition, other observables such as the higher order flow coefficients and v_1 can be incorporated into the Bayesian analysis, if permitted by computational constraints, for a more comprehensive constraint of the EOS in the future.

The authors thank Volker Koch, Behruz Kardan, and Shuzhe Shi for insightful discussions. This work is supported by the Helmholtzzentrum für Schwerionenforschung GSI (M. O. K.), the BMBF under the ErUM-Data and KISS projects (M. O. K., K. Z), the SAMSON AG (M. O. K., J. S., K. Z.) and the Walter Greiner Gesellschaft zur Förderung der physikalischen Grundlagenforschung e.V. through the Judah M. Eisenberg Laureatus Chair at the Goethe Universität Frankfurt am Main (H. S.).

*manjunath@fias.uni-frankfurt.de
†steinheimer@fias.uni-frankfurt.de
‡zhou@fias.uni-frankfurt.de
§stoecker@fias.uni-frankfurt.de

[1] Y. Aoki, G. Endrodi, Z. Fodor, S. D. Katz, and K. K. Szabo, Nature (London) **443**, 675 (2006).
[2] S. Borsanyi, G. Endrodi, Z. Fodor, A. Jakovac, S. D. Katz, S. Krieg, C. Ratti, and K. K. Szabo, J. High Energy Phys. 11 (2010) 077.
[3] J. N. Guenther, R. Bellwied, S. Borsanyi, Z. Fodor, S. D. Katz, A. Pasztor, C. Ratti, and K. K. Szabó, Nucl. Phys. **A967**, 720 (2017).
[4] M. A. Stephanov, Phys. Rev. Lett. **102**, 032301 (2009).
[5] M. A. Stephanov, Phys. Rev. Lett. **107**, 052301 (2011).
[6] M. Bluhm *et al.*, Nucl. Phys. **A1003**, 122016 (2020).
[7] H. Stoecker and W. Greiner, Phys. Rep. **137**, 277 (1986).
[8] J. Hofmann, H. Stoecker, U. W. Heinz, W. Scheid, and W. Greiner, Phys. Rev. Lett. **36**, 88 (1976).
[9] H. Stoecker, Nucl. Phys. **A750**, 121 (2005).
[10] M. A. Stephanov, K. Rajagopal, and E. V. Shuryak, Phys. Rev. Lett. **81**, 4816 (1998).
[11] Y. Hatta and M. A. Stephanov, Phys. Rev. Lett. **91**, 102003 (2003); **91**, 129901(E) (2003).
[12] S. Pratt, E. Sangaline, P. Sorensen, and H. Wang, Phys. Rev. Lett. **114**, 202301 (2015).
[13] L.-G. Pang, K. Zhou, N. Su, H. Petersen, H. Stöcker, and X.-N. Wang, Nat. Commun. **9**, 210 (2018).
[14] J. Steinheimer, L. Pang, K. Zhou, V. Koch, J. Randrup, and H. Stoecker, J. High Energy Phys. 12 (2019) 122.
[15] Y.-L. Du, K. Zhou, J. Steinheimer, L.-G. Pang, A. Motornenko, H.-S. Zong, X.-N. Wang, and H. Stöcker, Eur. Phys. J. C **80**, 516 (2020).
[16] L. Jiang, L. Wang, and K. Zhou, Phys. Rev. D **103**, 116023 (2021).
[17] M. Omana Kuttan, K. Zhou, J. Steinheimer, A. Redelbach, and H. Stoecker, J. High Energy Phys. 10 (2021) 184.
[18] D. Oliinychenko, A. Sorensen, V. Koch, and L. McLerran, Phys. Rev. C **108**, 034908 (2023).
[19] S. A. Bass *et al.*, Prog. Part. Nucl. Phys. **41**, 255 (1998).
[20] M. Bleicher *et al.*, J. Phys. G **25**, 1859 (1999).
[21] J. Aichelin and H. Stoecker, Phys. Lett. B **176**, 14 (1986).
[22] C. Hartnack, Z. X. Li, L. Neise, G. Peilert, A. Rosenhauer, H. Sorge, H. Stoecker, W. Greiner, and J. Aichelin, Nucl. Phys. **A495**, 303C (1989).
[23] J. Steinheimer, A. Motornenko, A. Sorensen, Y. Nara, V. Koch, and M. Bleicher, Eur. Phys. J. C **82**, 911 (2022).
[24] This simplification can be supported by the fact that at the beam energies under investigation, the EOS is dominated by the contribution from baryons.
[25] M. Omana Kuttan, A. Motornenko, J. Steinheimer, H. Stoecker, Y. Nara, and M. Bleicher, Eur. Phys. J. C **82**, 427 (2022).
[26] I. Tews, T. Krüger, K. Hebeler, and A. Schwenk, Phys. Rev. Lett. **110**, 032504 (2013).
[27] C. Drischler, K. Hebeler, and A. Schwenk, Phys. Rev. Lett. **122**, 042501 (2019).
[28] Y. Wang, C. Guo, Q. Li, A. Le Fèvre, Y. Leifels, and W. Trautmann, Phys. Lett. B **778**, 207 (2018).
[29] P. Danielewicz, R. Lacey, and W. G. Lynch, Science **298**, 1592 (2002).
[30] H. Kruse, B. V. Jacak, and H. Stoecker, Phys. Rev. Lett. **54**, 289 (1985).
[31] J. Molitoris and H. Stoecker, Phys. Lett. **162B**, 47 (1985).
[32] S. Huth *et al.*, Nature (London) **606**, 276 (2022).
[33] C. Pinkenburg *et al.* (E895 Collaboration), Phys. Rev. Lett. **83**, 1295 (1999).
[34] D. Adamova *et al.* (CERES Collaboration), Nucl. Phys. **A698**, 253 (2002).
[35] A. Andronic *et al.* (FOPI Collaboration), Phys. Lett. B **612**, 173 (2005).
[36] L. Adamczyk *et al.* (STAR Collaboration), Phys. Rev. C **86**, 054908 (2012).
[37] J. Adam *et al.* (STAR Collaboration), Phys. Rev. C **103**, 034908 (2021).
[38] J. Adamczewski-Musch *et al.* (HADES Collaboration), Phys. Rev. Lett. **125**, 262301 (2020).
[39] M. S. Abdallah *et al.* (STAR Collaboration), Phys. Lett. B **827**, 137003 (2022).
[40] L. Ahle *et al.* (E802 Collaboration), Phys. Rev. C **60**, 064901 (1999).
[41] C. Alt *et al.* (NA49 Collaboration), Phys. Rev. C **73**, 044910 (2006).
[42] L. Adamczyk *et al.* (STAR Collaboration), Phys. Rev. C **96**, 044904 (2017).
[43] Y. Nara, H. Niemi, J. Steinheimer, and H. Stöcker, Phys. Lett. B **769**, 543 (2017).
[44] See Supplemental Material at http://link.aps.org/supplemental/10.1103/PhysRevLett.131.202303 for detailed technical discussions on the data used, the Gaussian process models, bayesian inference procedures, closure tests and additional tests on the extracted equations of state.
[45] T. Reichert, J. Steinheimer, C. Herold, A. Limphirat, and M. Bleicher, Eur. Phys. J. C **82**, 510 (2022).
[46] C. Currin, T. Mitchell, M. Morris, and D. Ylvisaker, J. Am. Stat. Assoc. **86**, 953 (1991).
[47] J. E. Bernhard, J. S. Moreland, and S. A. Bass, Nat. Phys. **15**, 1113 (2019).
[48] J. Novak, K. Novak, S. Pratt, J. Vredevoogd, C. E. Coleman-Smith, and R. L. Wolpert, Phys. Rev. C **89**, 034917 (2014).
[49] https://www.pymc.io/projects/docs/en/v4.1.6/api/generated/pymc.DEMetropolisZ.html, accessed: 2022-09-01.
[50] C. J. Ter Braak and J. A. Vrugt, Stat. Comput. **18**, 435 (2008).
[51] https://github.com/pymc-devs/pymc/releases/tag/v4.0.0, accessed: 2022-09-01.
[52] O. Savchuk, A. Motornenko, J. Steinheimer, V. Vovchenko, M. Bleicher, M. Gorenstein, and T. Galatyuk, arXiv:2209.05267.
[53] P. Li, J. Steinheimer, T. Reichert, A. Kittiratpattana, M. Bleicher, and Q. Li, Sci. China Phys. Mech. Astron. **66**, 232011 (2023).
[54] O. Savchuk, R. V. Poberezhnyuk, A. Motornenko, J. Steinheimer, M. I. Gorenstein, and V. Vovchenko, Phys. Rev. C **107**, 024913 (2023).

[55] T. Reichert, O. Savchuk, A. Kittiratpattana, P. Li, J. Steinheimer, M. Gorenstein, and M. Bleicher, Phys. Lett. B **841**, 137947 (2023).
[56] J. Adamczewski-Musch *et al.* (HADES Collaboration), Eur. Phys. J. A **59**, 80 (2023).
[57] M. S. Abdallah *et al.* (STAR Collaboration), Phys. Lett. B **827**, 136941 (2022).
[58] E. Kashirin, I. Selyuzhenkov, O. Golosov, and V. Klochkov (NA61/Shine Collaboration), J. Phys. Conf. Ser. **1690**, 012127 (2020).
[59] J. Barrette *et al.* (E877 Collaboration), Phys. Rev. C **55**, 1420 (1997); **56**, 2336(E) (1997).
[60] C. Alt *et al.* (NA49 Collaboration), Phys. Rev. C **68**, 034903 (2003).
[61] S. Altiparmak, C. Ecker, and L. Rezzolla, Astrophys. J. Lett. **939**, L34 (2022).
[62] Note, that even though the two systems have a different isospin fraction, the effect of the isospin composition is likely small at large densities.
[63] S. Soma, L. Wang, S. Shi, H. Stöcker, and K. Zhou, Phys. Rev. D **107**, 083028 (2023).
[64] M. Leonhardt, M. Pospiech, B. Schallmo, J. Braun, C. Drischler, K. Hebeler, and A. Schwenk, Phys. Rev. Lett. **125**, 142502 (2020).
[65] Y. Fujimoto, K. Fukushima, L. D. McLerran, and M. Praszalowicz, Phys. Rev. Lett. **129**, 252702 (2022).
[66] A. Sorensen *et al.*, arXiv:2301.13253.